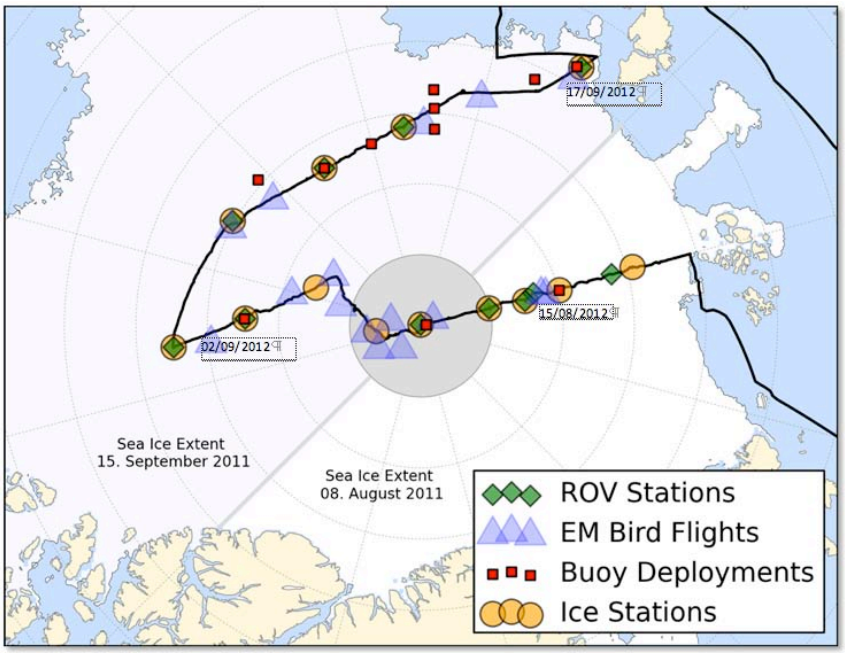

Figure 1. Cruise track of the Polarstern expedition TransArc (ARK-XXVI/3, 2012) to the Arctic Ocean. Symbols indicate the type of measurement performed along the cruise track. Source: Schauer (2012).

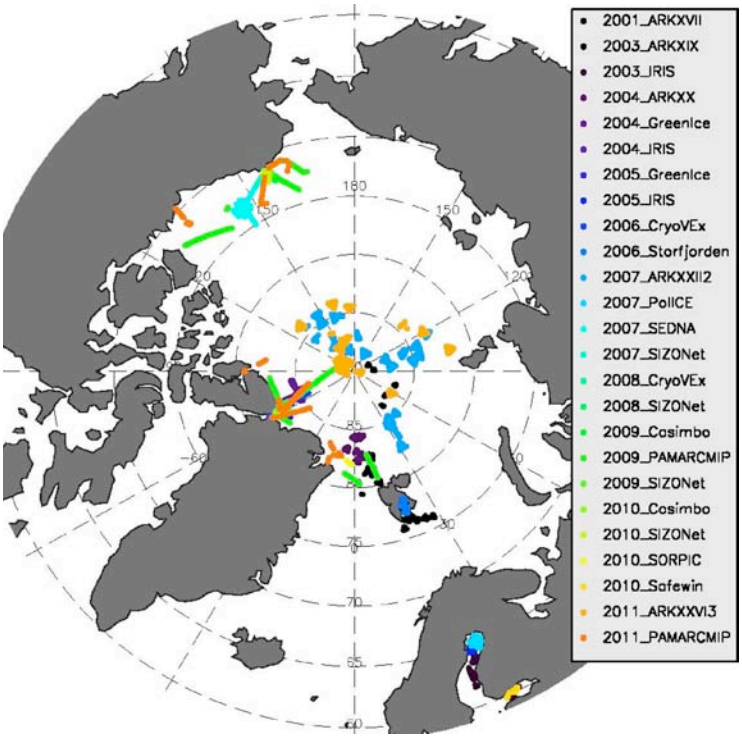

a

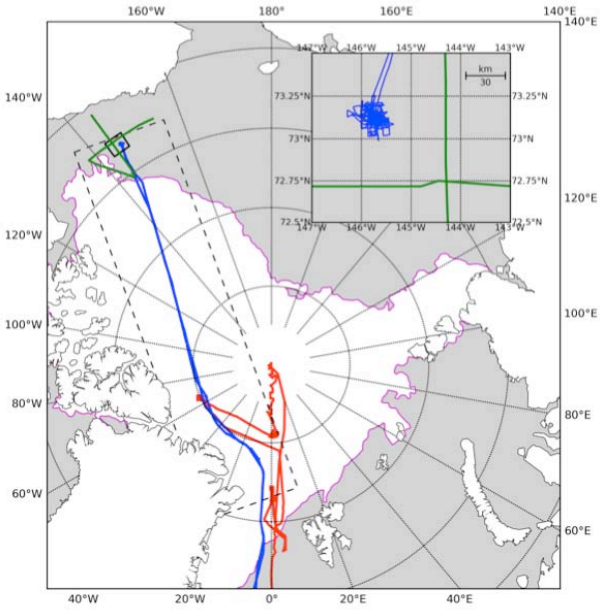

b

Figure 2 (a): Map of airborne EM surveys conducted by AWI since 2001 ; (b) Map of UK submarine transects in 2004 (red) and 2007 (blue)

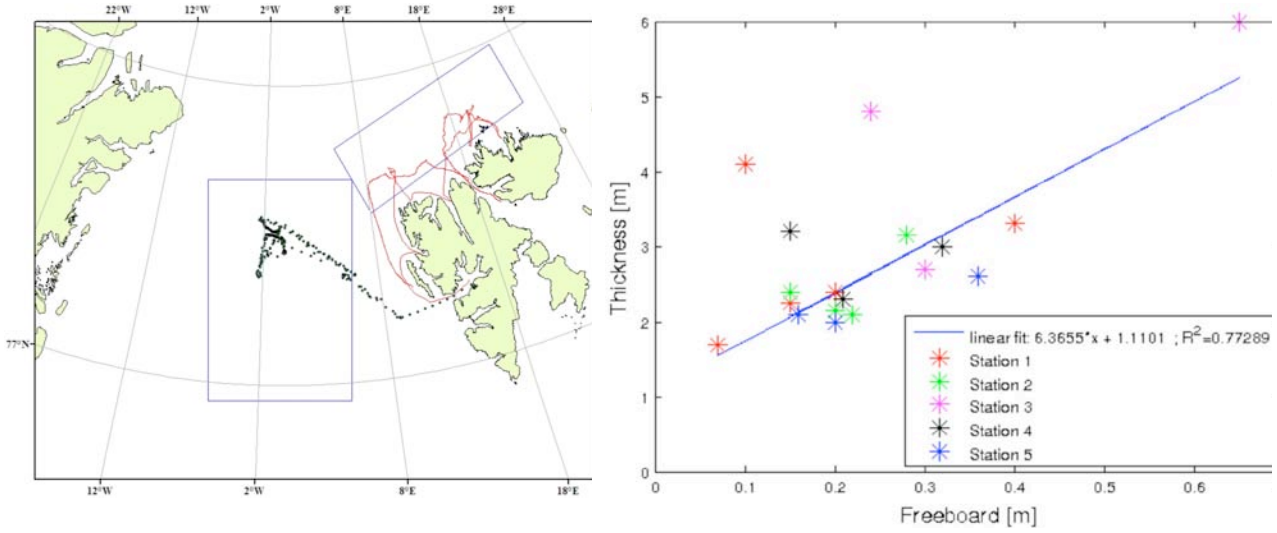

a b

Figure 3. (a) map of KV Svalbard tracks in April (red lines) and September (black dots) 2011. (b): Thickness versus freeboard for FY ice in the Fram Strait in September 2011.

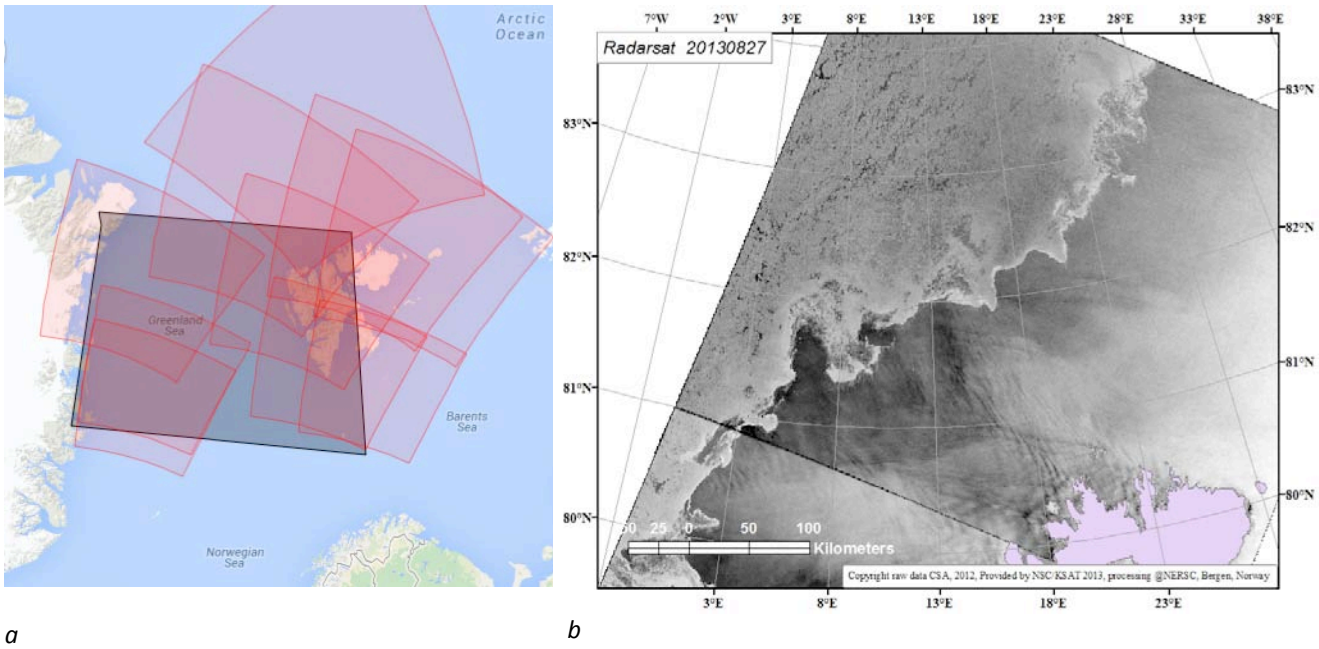

a *b*

Figure 5. Example of SAR data provided by GMES for use in the project. (a) Coverage of 10 Radarsat SacSAR scenes from 1 – 3 May 2012; (b) Radarsat ScanSAR image north of Svalbard geolocated on map projection.

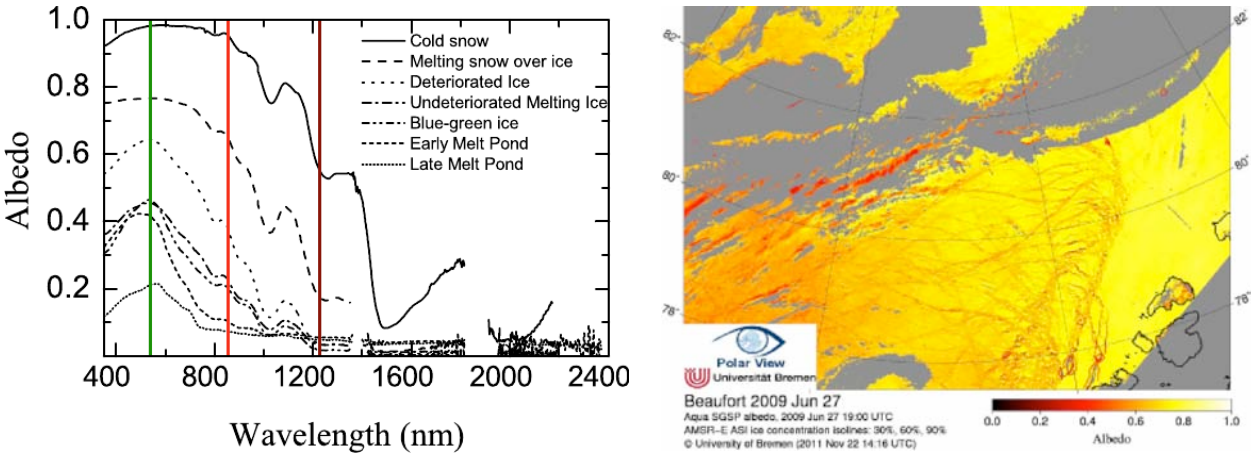

a b

Figure 6. (a) Spectral albedos of various surface types, from cold snow to late metlpond (Source: Grenfell, Perovich, 2004). Vertical lines correspond to MODIS channels: green – band 4 (545-565nm), red – band 2 (841-876nm), brown – band 5 (1230-1250nm). (b) Preliminary sea ice albedo retrieval product composed of an average of MODIS bands 1,2,3 (clouds are screened out using MODIS cloud mask).

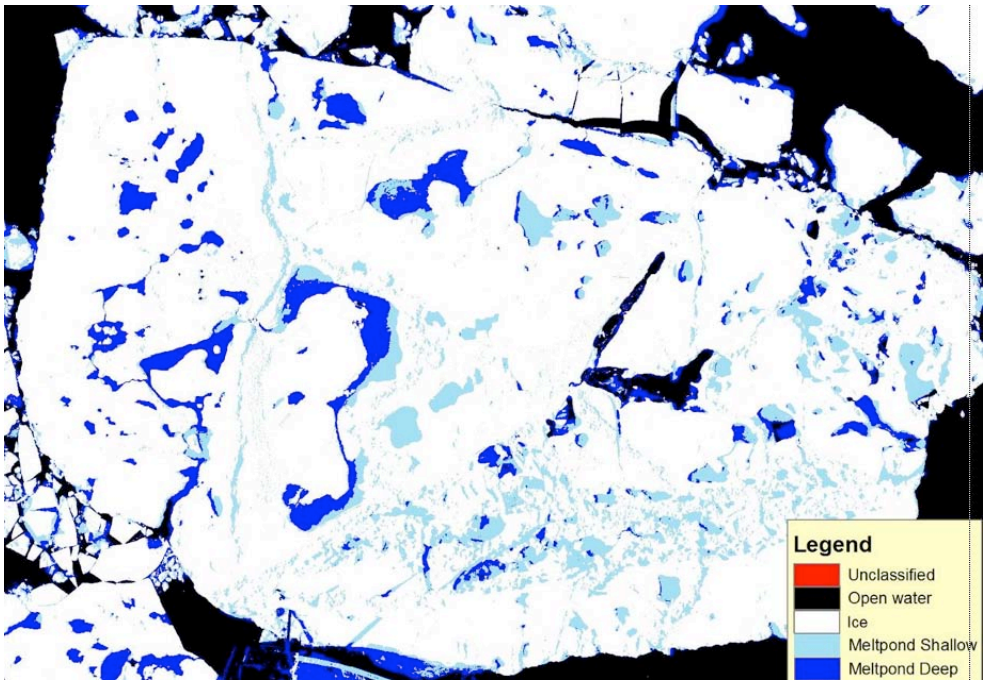

Figure 7. Example of supervised melt pond classification for the validation of the melt pond fraction retrieval algorithm. Open water (black), ice (white), ponds on thin ice (dark blue) and ponds on thick ice (light blue) are classified (Courtesy T. Krumpen, AWI).

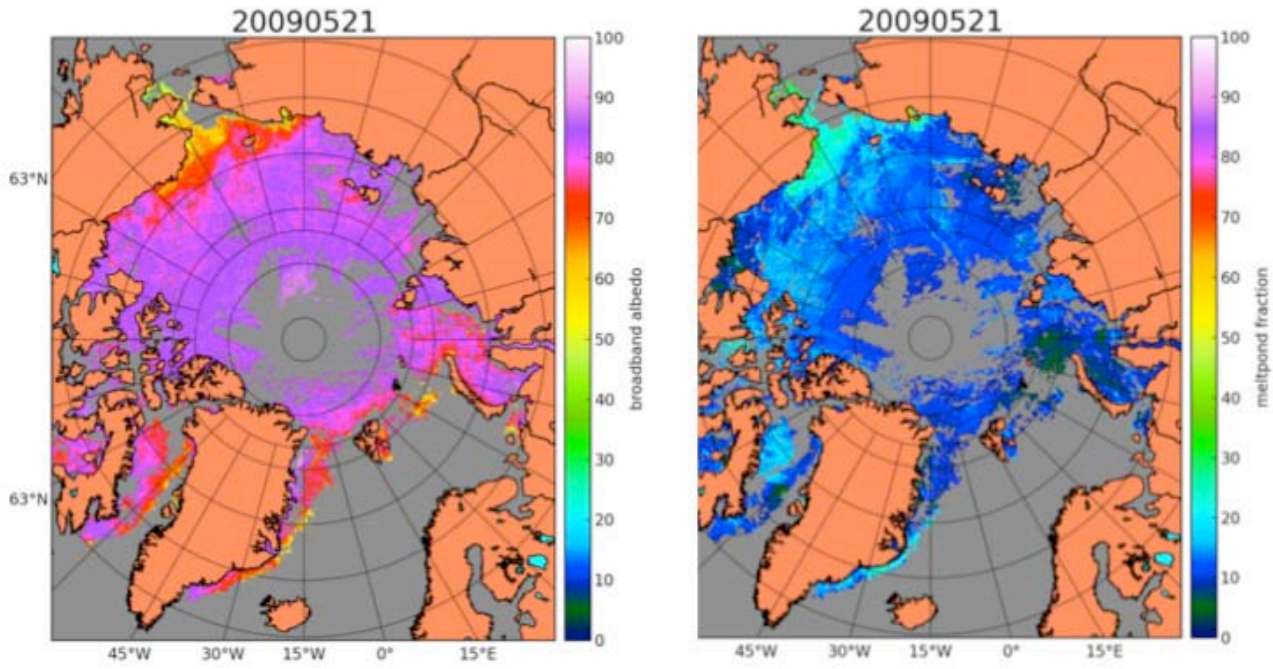

Figure 8: Daily maps of albedo (left) and meltpond fraction for 21 May 2009. Grey area are covered by clouds or open water.

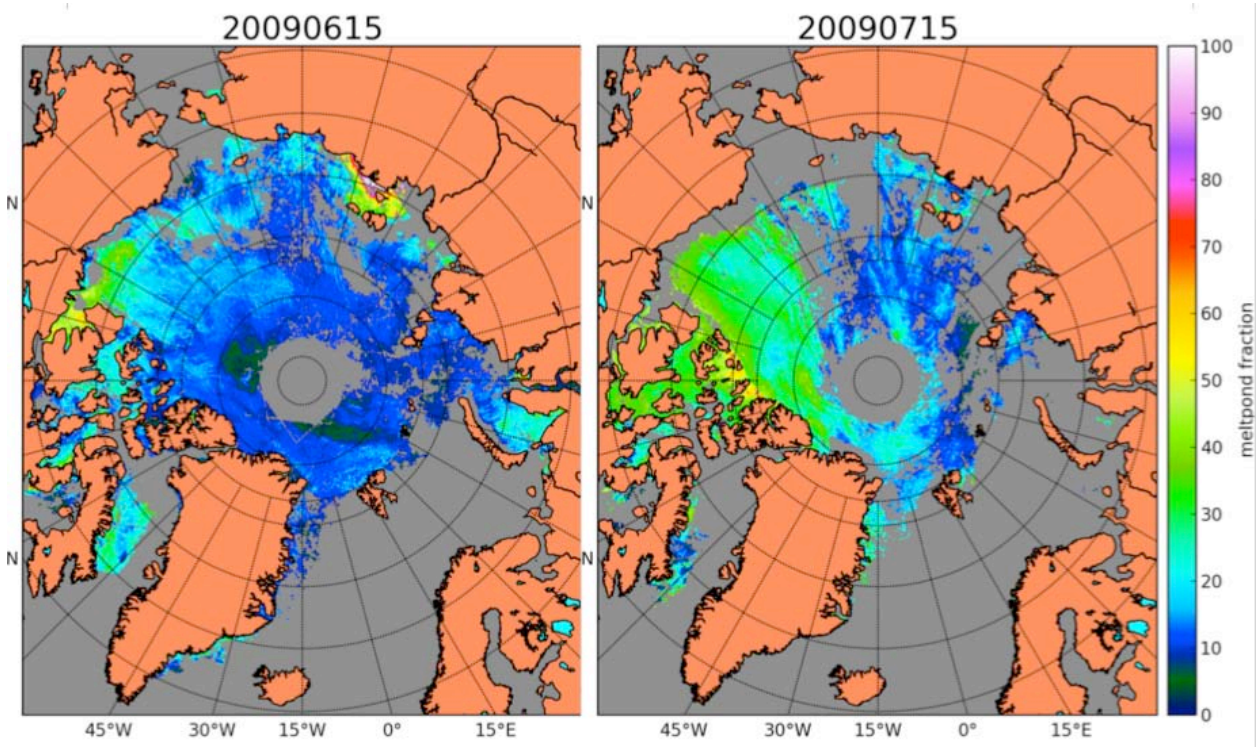

Figure 9. Example of Arctic meltpond fraction maps based on weekly averaged data for the a week in June 2009 (left) and 2011 (right).

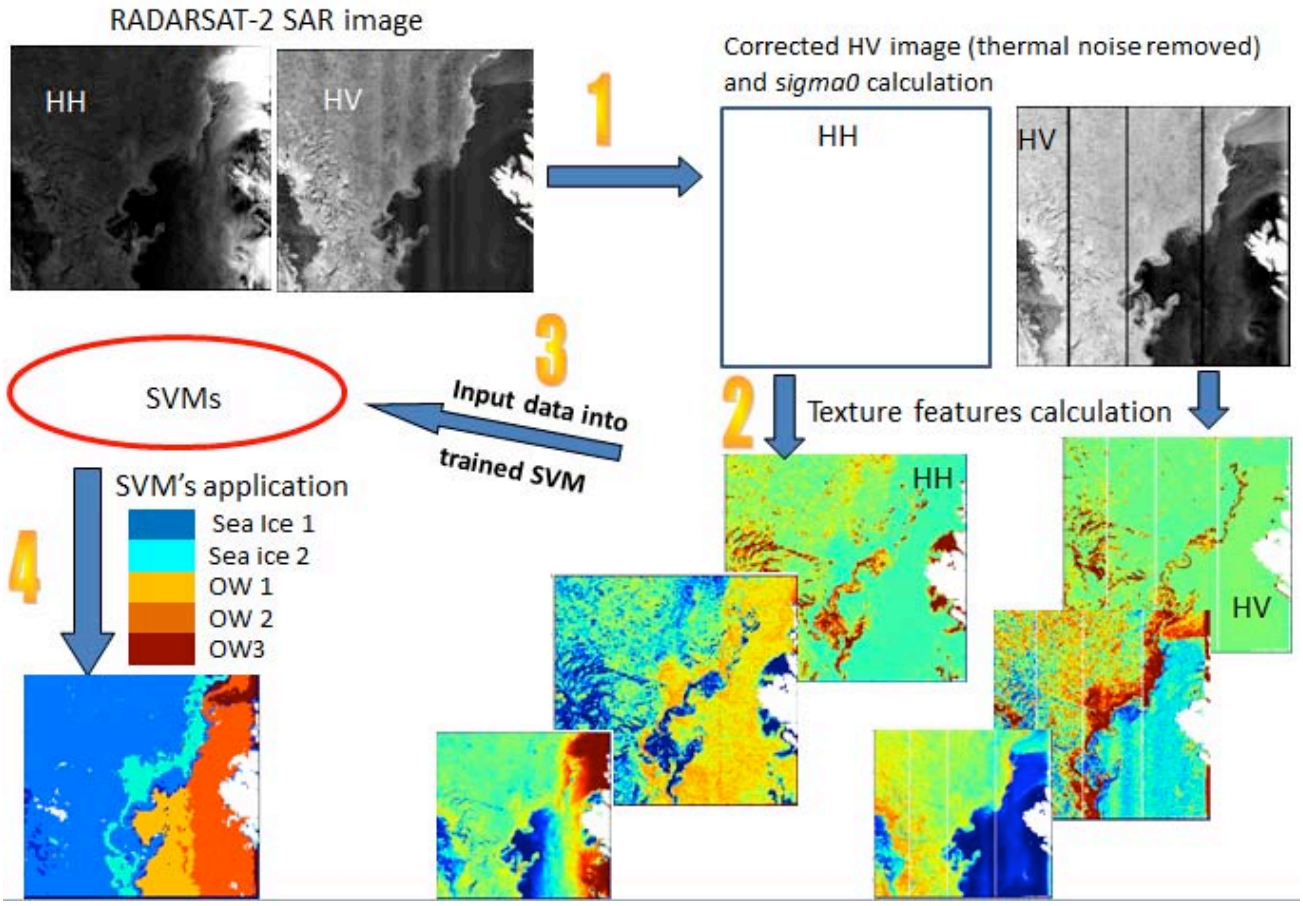

Figure 10. The processing step of the SVMs classification procedure for ice type classification of Radarsat-2 dual polarization SAR images.

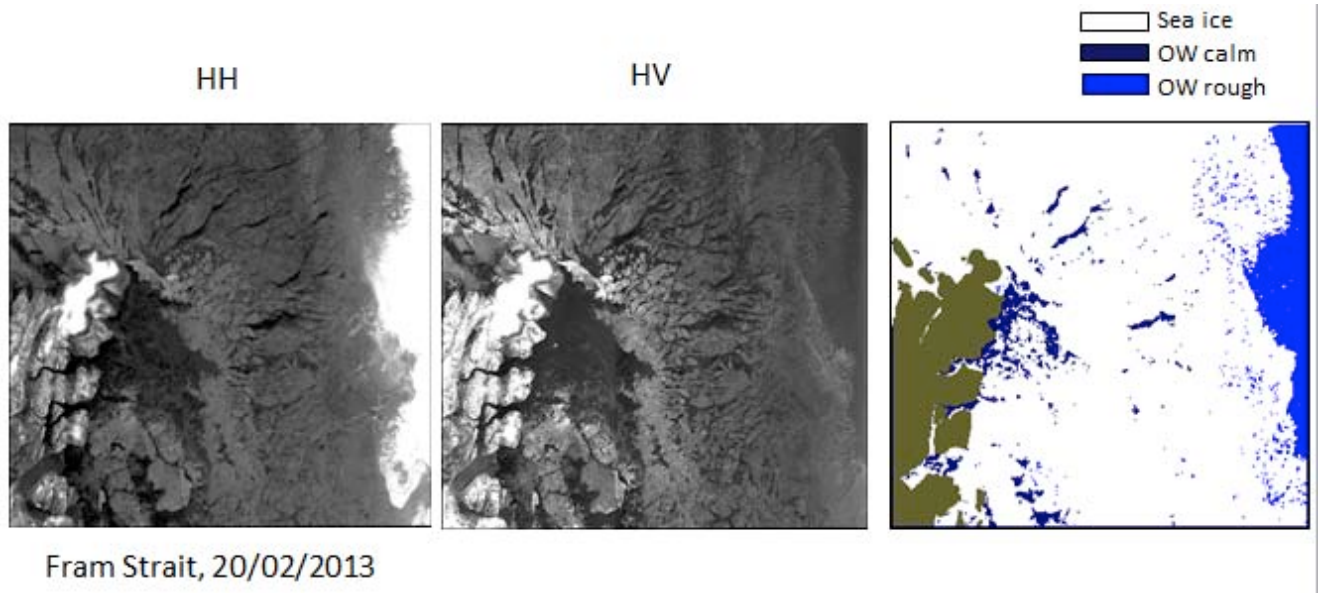

Figure 11. Example of SVMs classification result in the Fram Strait where open water and sea ice is separated.

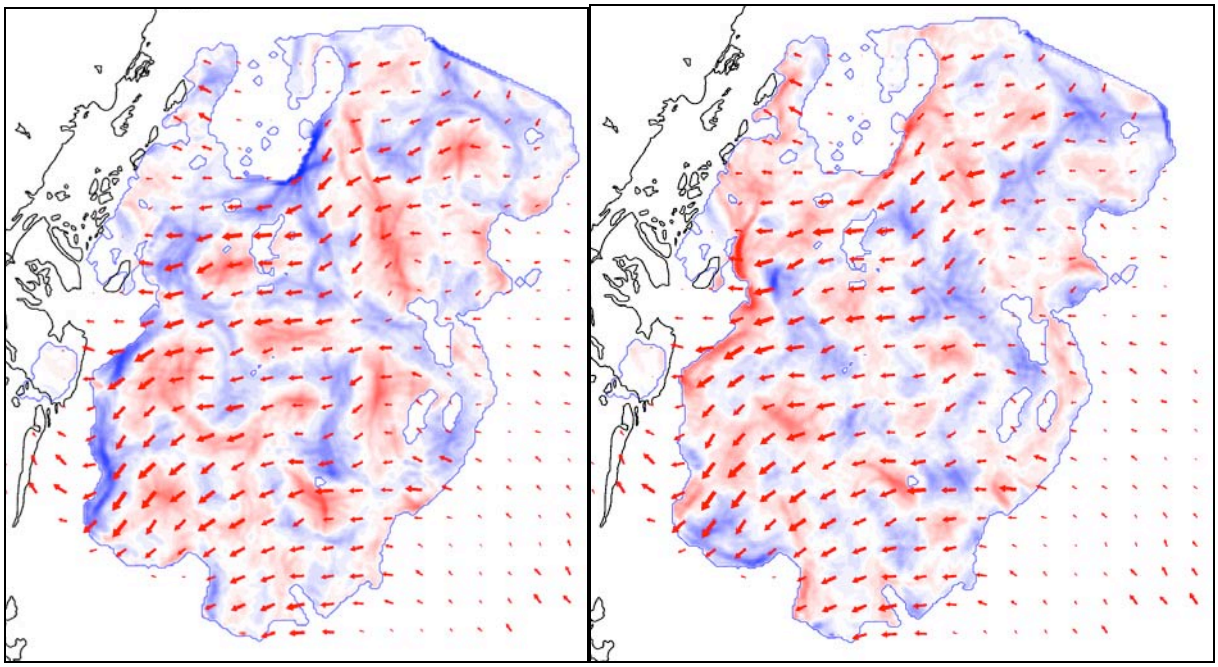

Figure 12: Presentation of results: here to the left zones of divergence (blue) and convergence (red), and to the right vorticity (the colors indicate whether the vortictiy is positive or negative). .

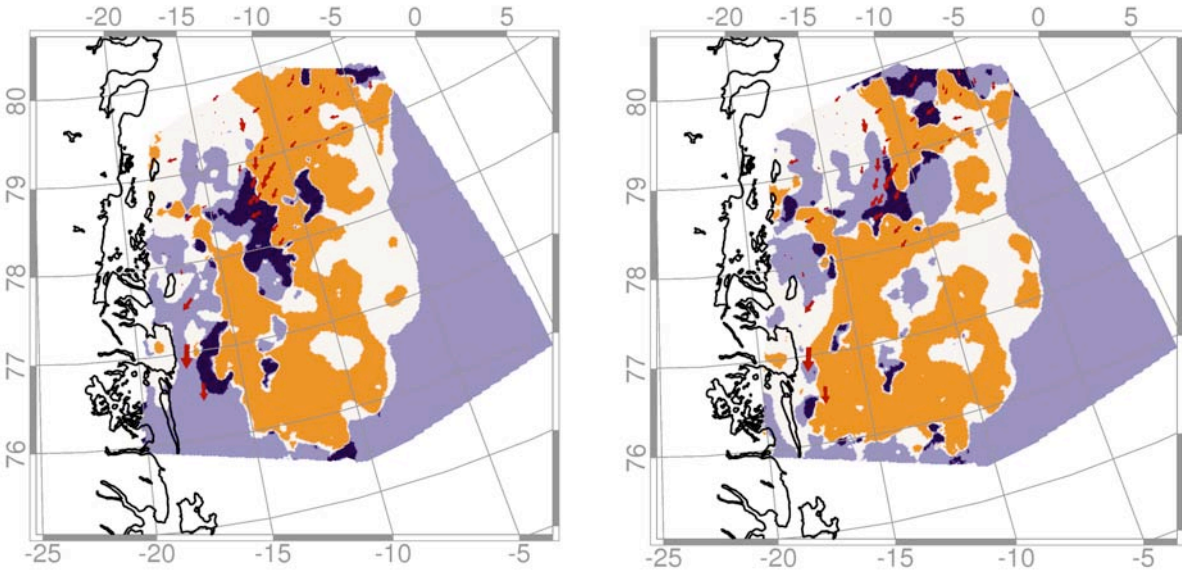

Figure 13: Quality maps for the motion field derived from a pair of Radarsat-2 images acquired on 2012/09/16. Left: HH polarization; Right: HV polarization.

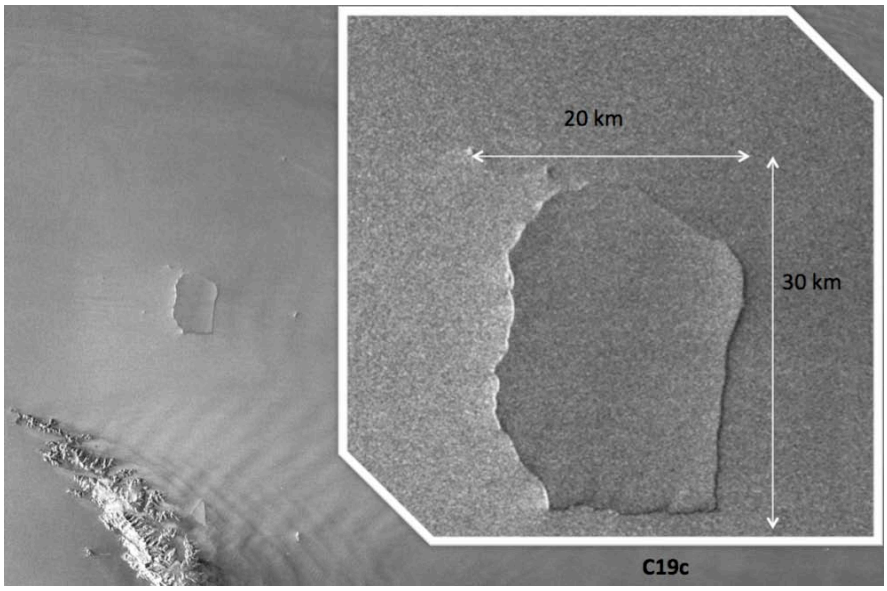

Figure 14. Example of SAR detection of a large iceberg in Antarctica, with size of 20 by 30 km, and identification of several smaller icebergs in the neighborhood.

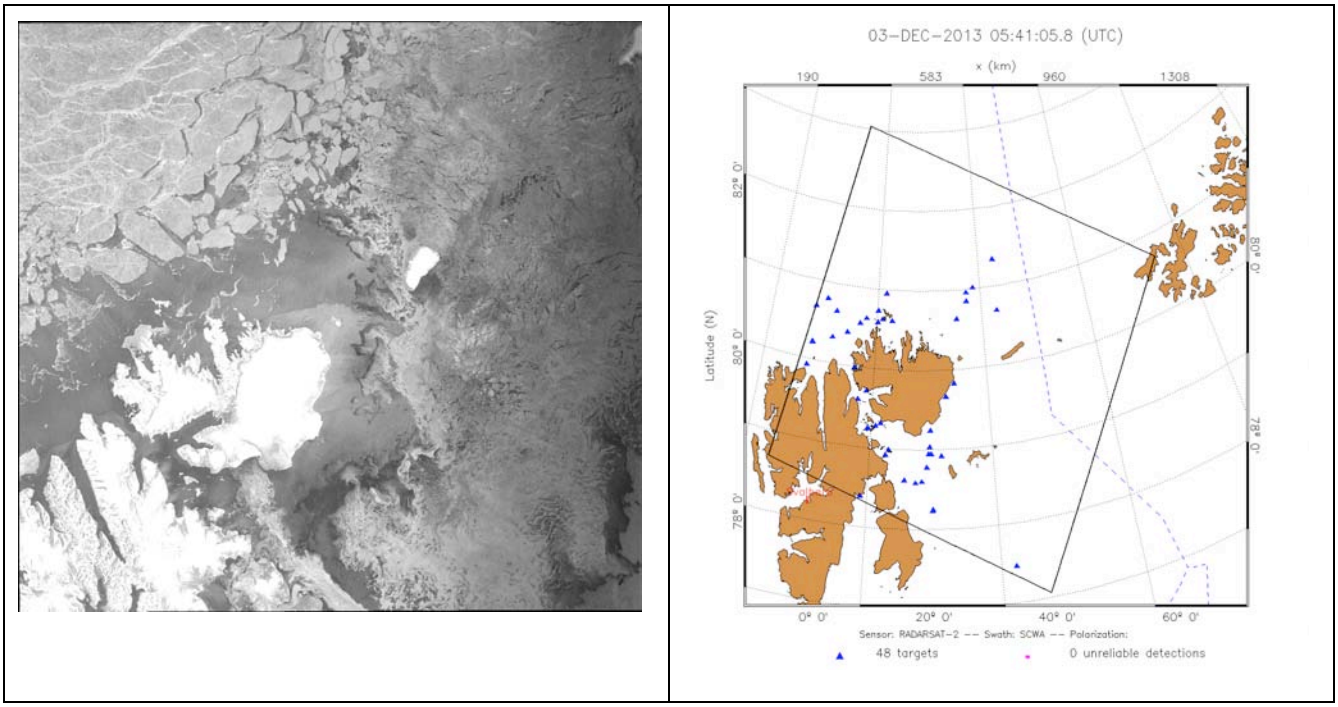

Figure 15. Example of difficulties of SAR detection of icebergs in the Svalbard area where drifting sea ice is the dominating feature in the SAR image. Left: SAR image; Right : Bright target detection with the non-parametric detector with p=0.01%. Note that the results are not validated.

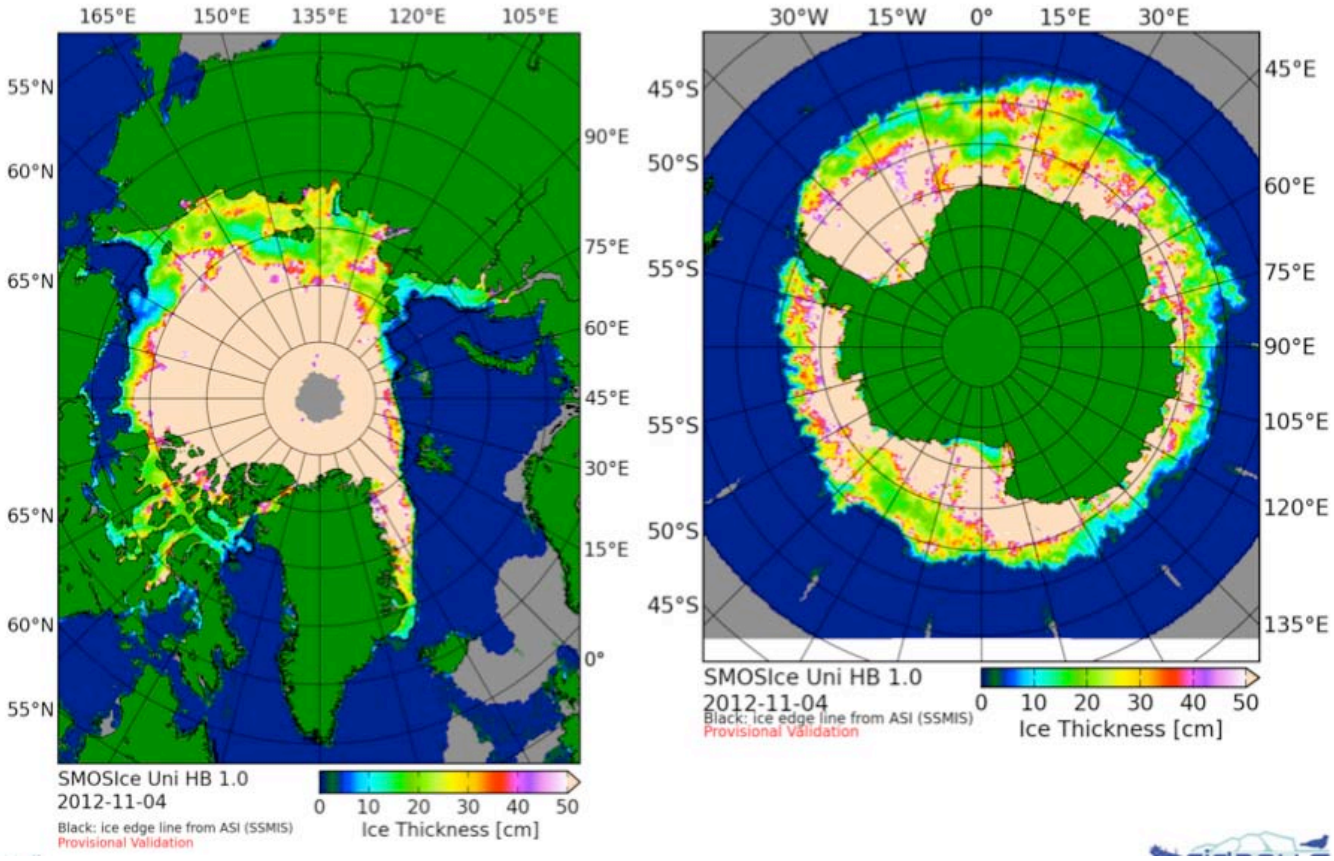

Figure 16. Example of thin ice thickness maps for the Arctic and Antarctic using L-band passive microwave data from SMOS.

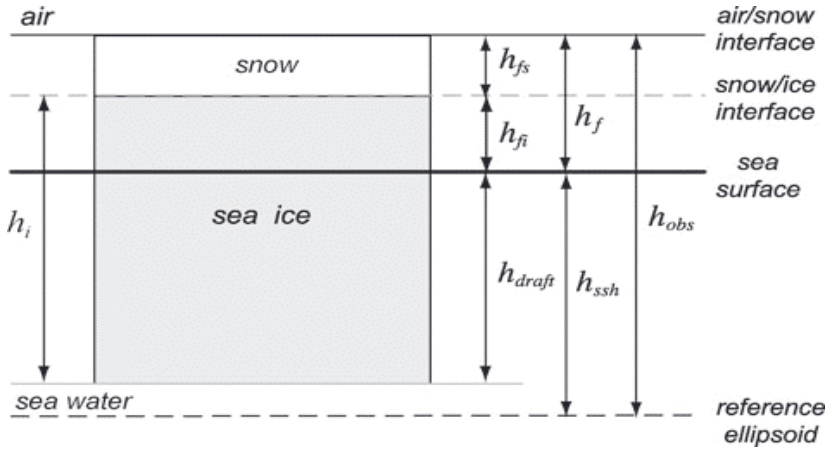

Figure 17: Computation of sea ice thickness from ice freeboard measured by radar and laser altimeter.

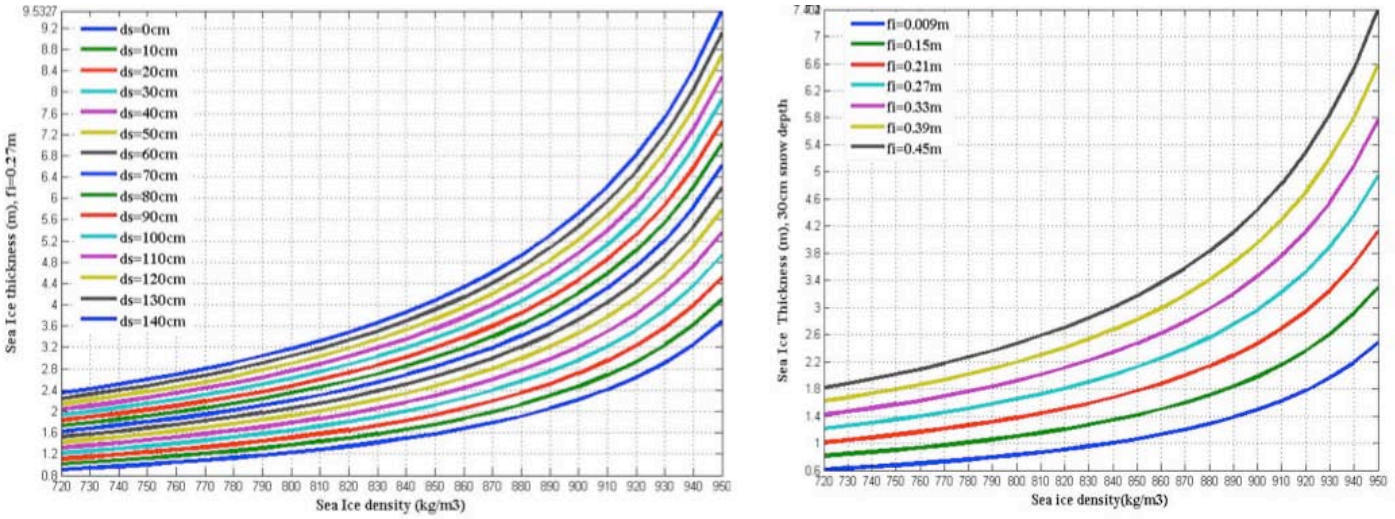

Figure 18. Left: Sensitivity of SIT to sea ice density and snow depth; right: sensitivity of the retrieved SIT on ice density for snow depth 30cm and free-board change from 0.09m to 0.45m.

Validation of ice thickness retrievals from radar altimeter data from ERS and ENVISAT

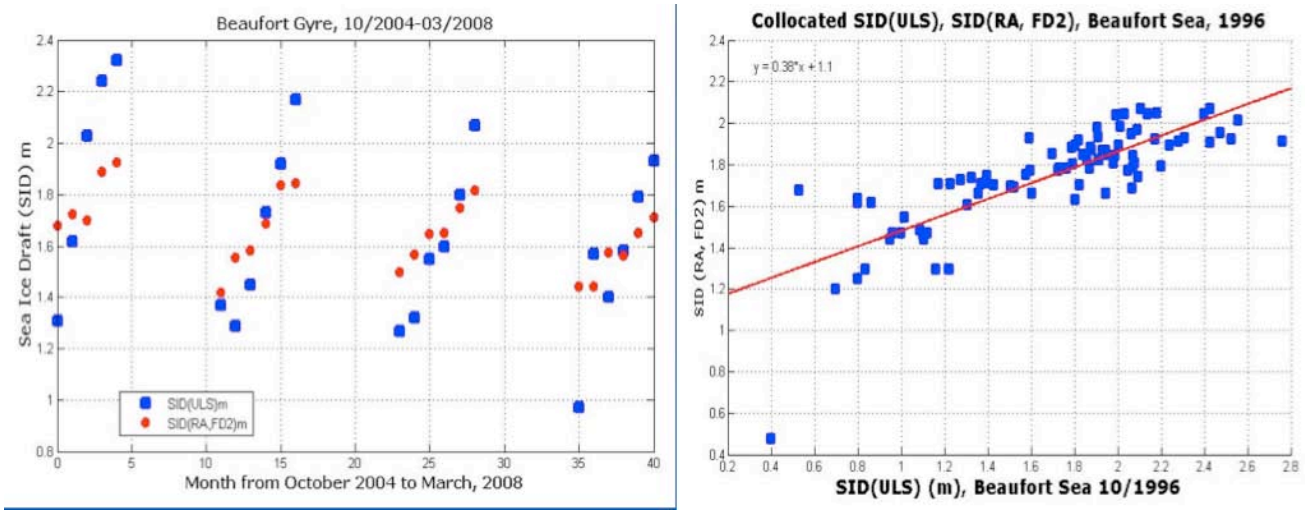

Figure 19. Left: Comparison of ice draft retrieved from ENVISAT radar altimeter (red dots) and ULS data (blue dots) based on monthly mean values for October to March 2004 to 2008. Right: Plot of collocated data from Radar Altimeter from ERS versus ULS from submarine surveys in the Beaufort Sea in October 1996.

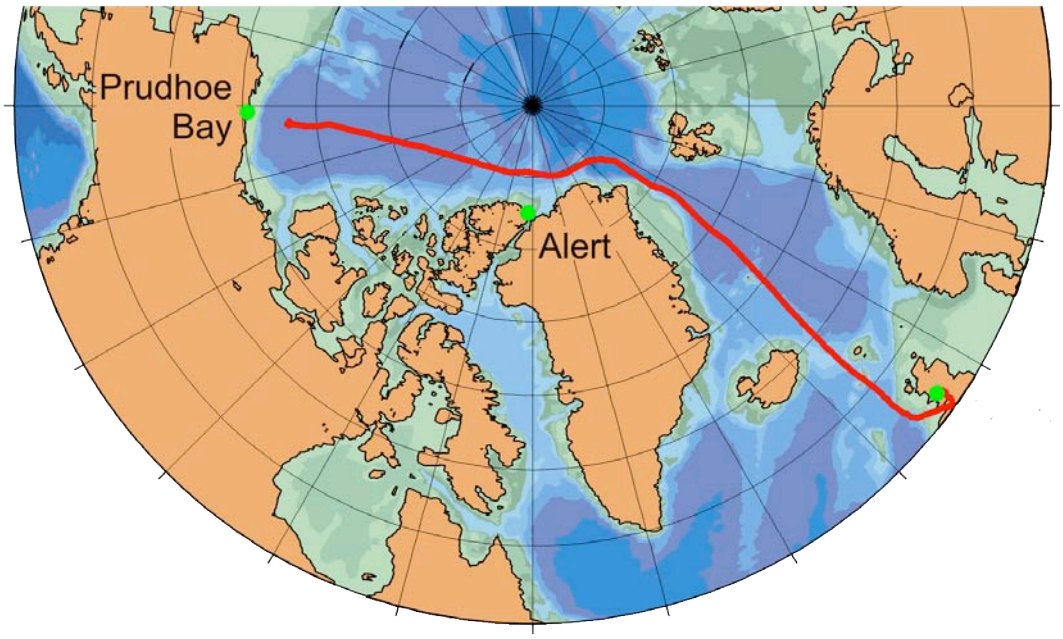

Figure 20. Transect across the Arctic with UK submarine "Tireless" in March – April 2007, collecting Upward-Looking Sonar data of ice draft

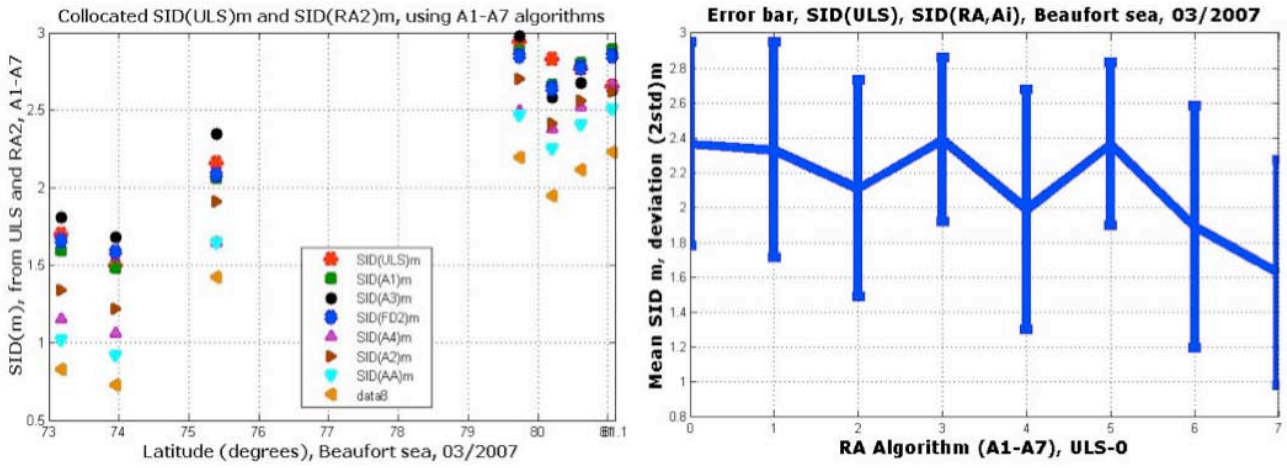

Figure 21. Left: Comparison of seven ice thickness retrieval algorithms for satellite radar altimeter data with data from seven locations from submarine ULS data in Beaufort Sea in March 2007. Right: Mean and standard deviation of the algorithms compared to the ULS data.

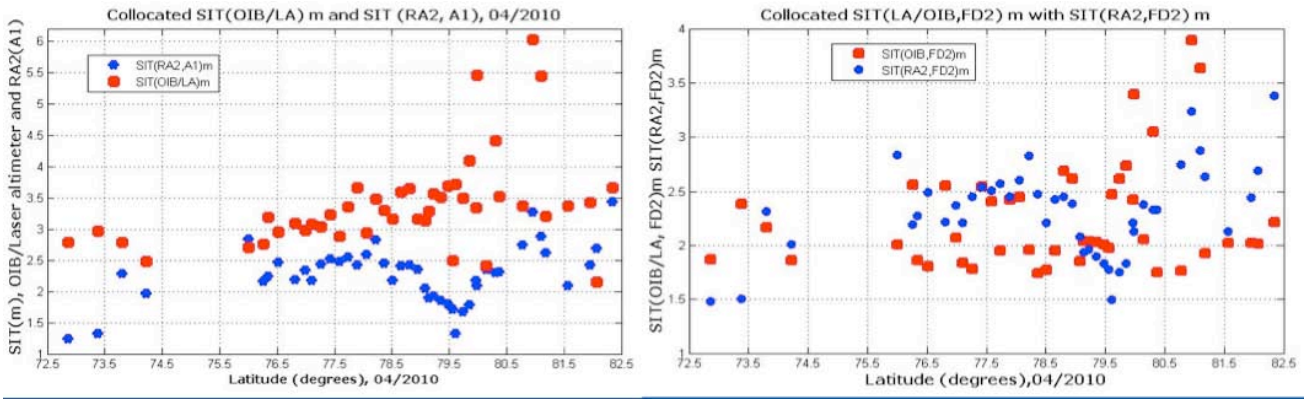

Figure 22. Comparison of a profile of ice thickness (SIT) from ENVISAT radar altimeter (blue dots) and derived thickness laser altimeter from Operation Ice Bridge (OIB). Left: retrieval using the A1 radar algorithm, right: retrieval using the FD2 radar algorithm.

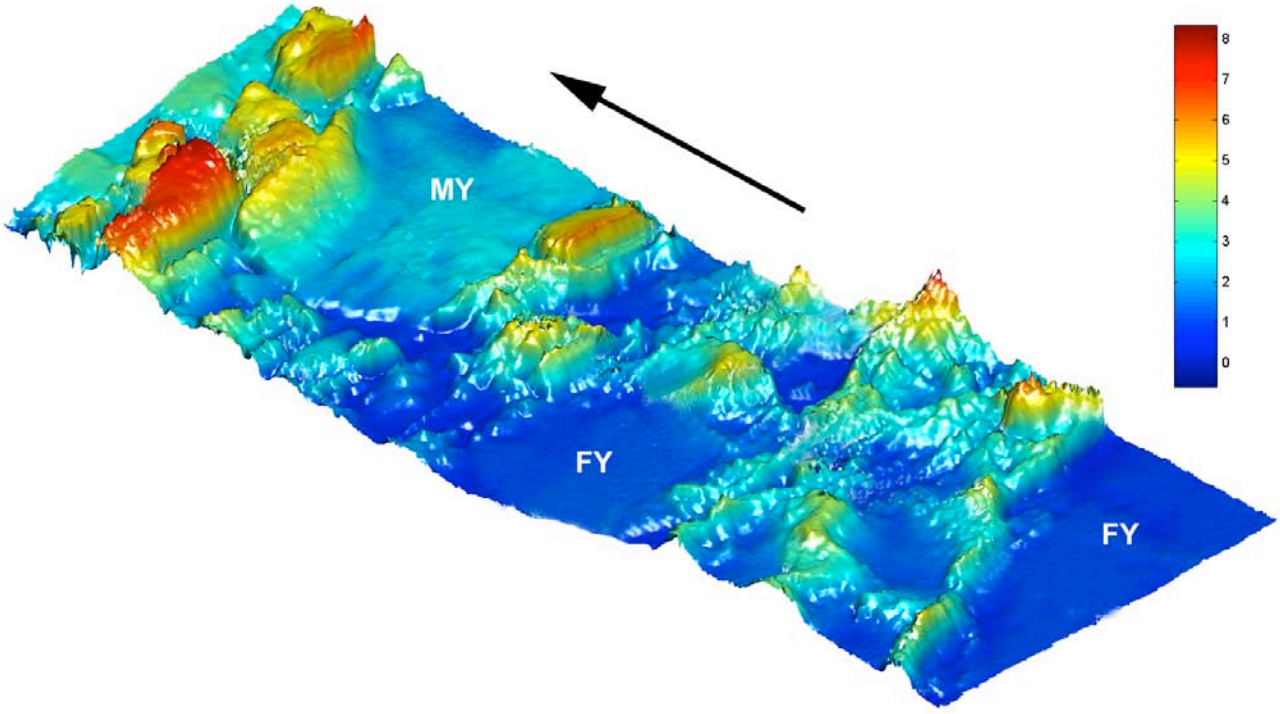

Figure 23. Example of AUV mapping of the ice draft using scanning upward-looking sonar (ULS) in an area where both multiyear and firstyear ice is present. Ice draft data are important to study the relation between thickness retrievals from freeboard measurements and direct thickness measurements from ULS surveys. The colour code shows the draft in meter.

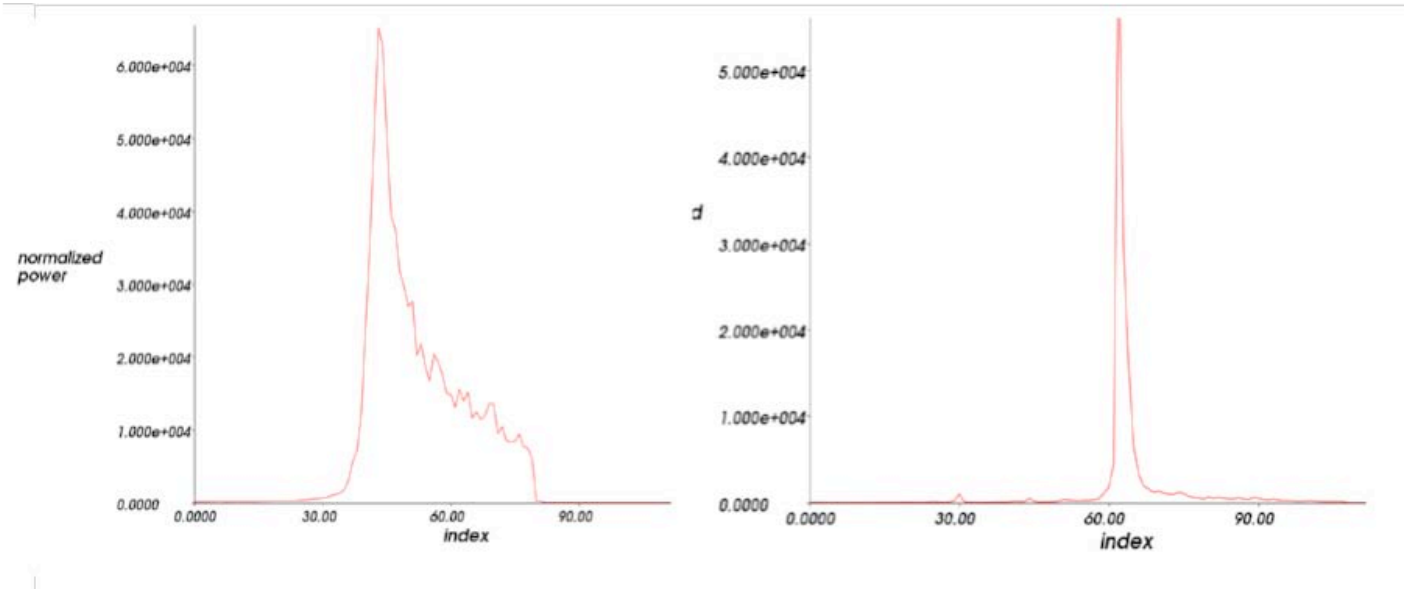

Figure 24. Waveforms in SAR mode over ocean (left) and over ice (right).

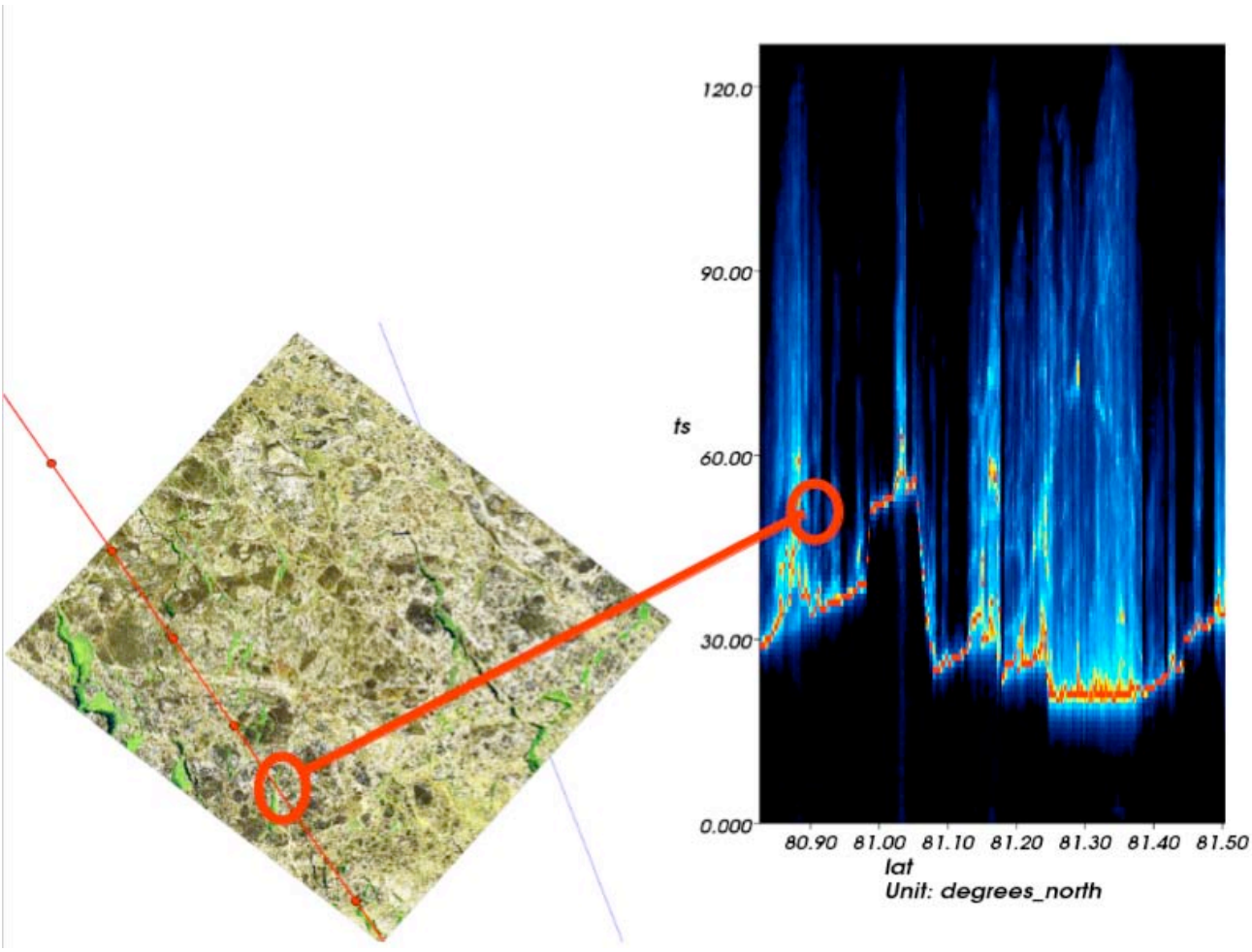

Figure 25. Data obtained on 13 April 2011 showing a Radarsat-2 image (left) and CryoSat-2 level 1b waveform transect (right). The red transect line shows how the waveform could be used to detect thin level ice or leads.

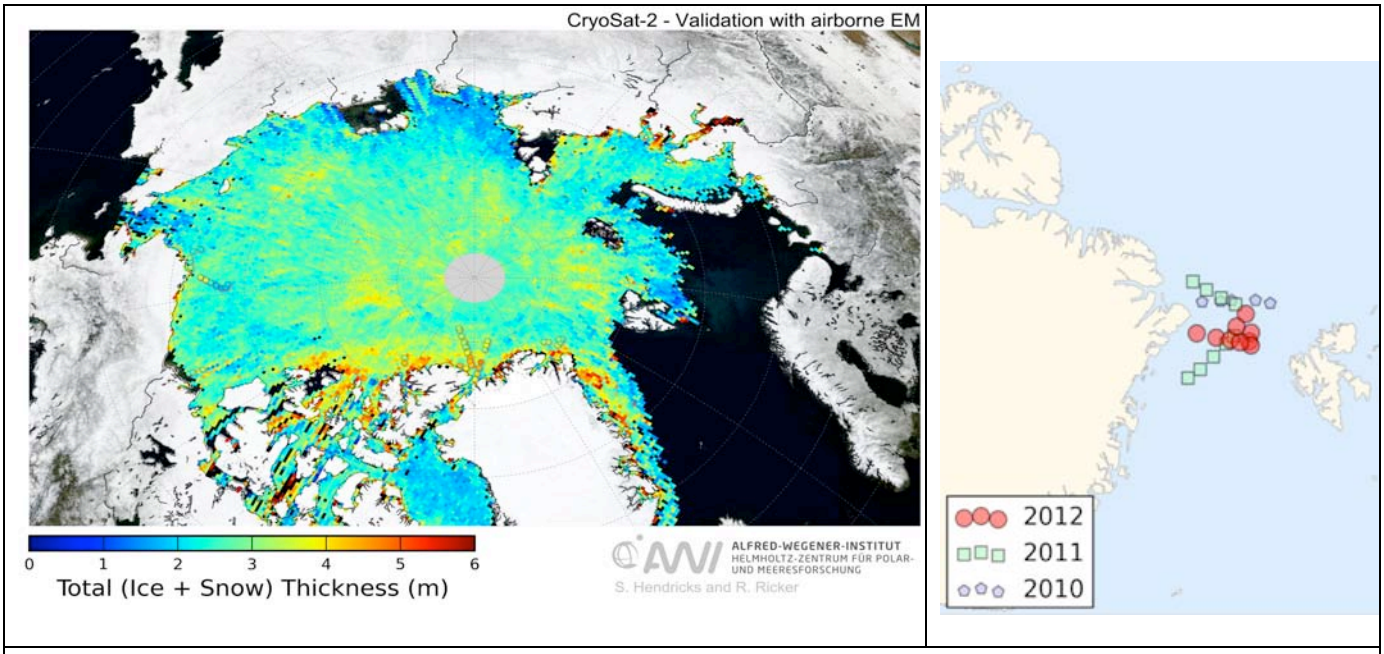

Figure 26. Radar altimeter data from CryoSat-2 can be used to estimate total thickness in the Arctic. The thickness is calculated from ice freeboard data collected by the satellite. The example above shows the monthly mean ice thickness for March 2011. Flightlines of airborne electromagnetic surveys (EM data) from the AWI field campaign PAMARCMIP/CryoVEx 2011 are superimposed. The map to the right shows EM flights in the Fram Strait during validation campaigns. The EM data are compared to the satellite retrievals and used for validation. The data is freely available at http://www.meereisportal.de

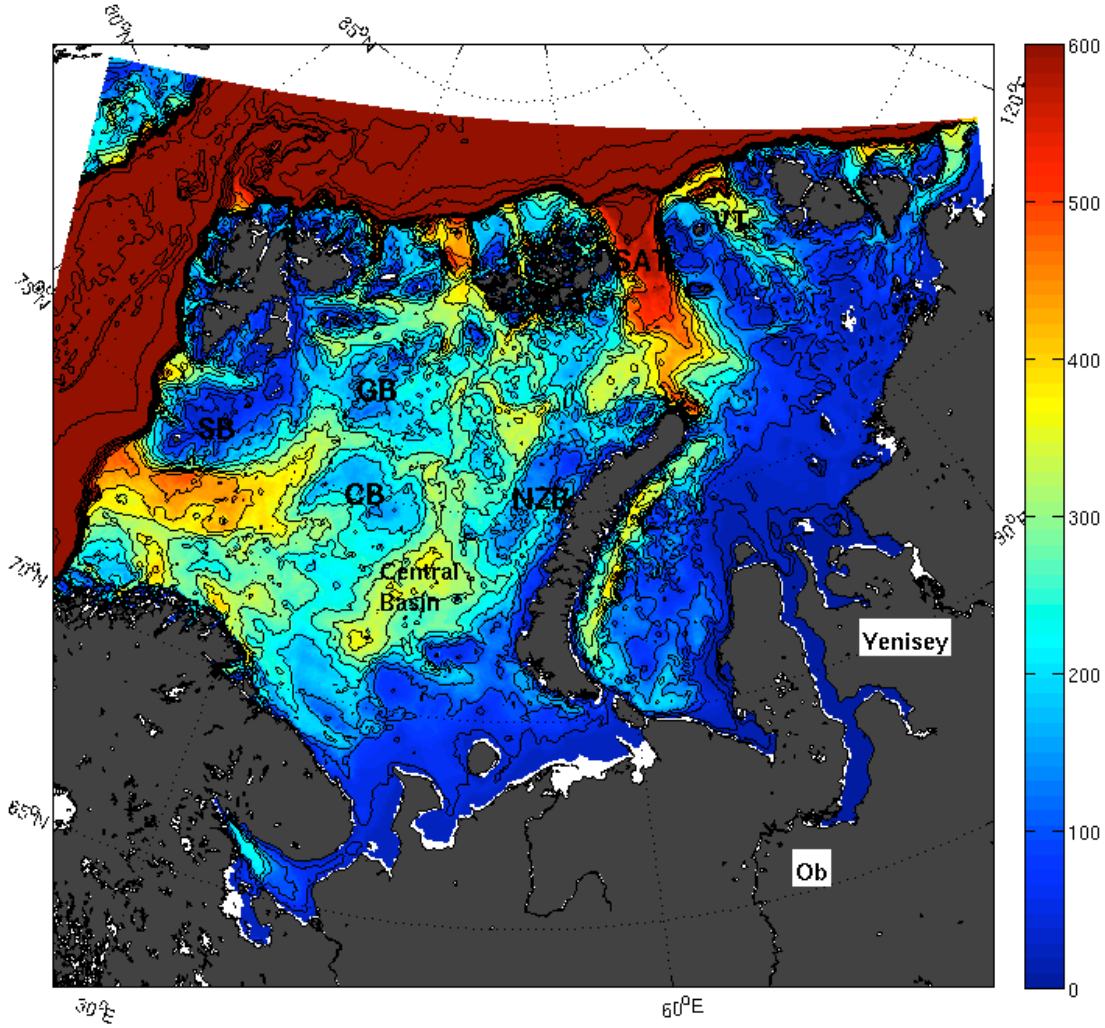

Figure 27. Bathymetry used in the Barents and Kara Sea model, with the larges rivers, Ob and Yenisey, indicated as well as the Central Basin, Central Bank (CB), Great Bank (GB), Svalbard Bank (SB), Novaya Zemlya Bank (NZB), St. Anna Trough (ST), and Veronin Trough (VT). The colour scale is limited down to 600 m depth to highlight the bathymetry on the shelf. Non-coloured areas are outside the model domain and indicate the open boundaries in the north and the west.

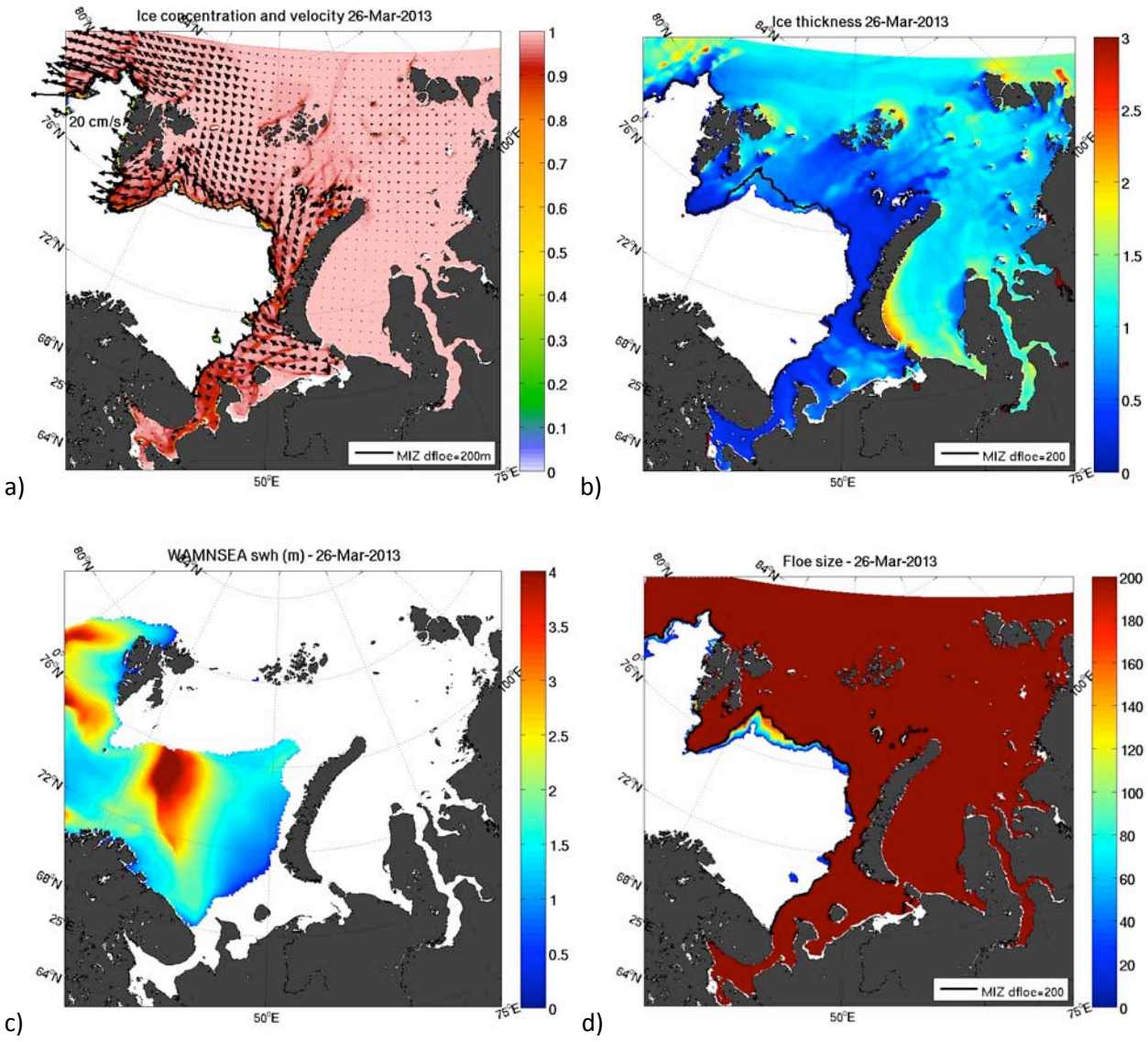

Figure 18. Forecast with the WIM forecast model for the 26th of Mars 2013, a) sea ice concentration and velocity, b) sea ice thickness (m), c) significant wave height (m) from met.no (WAMNSEA10km), and d) maximum floe size (m) produced by the WIM module.

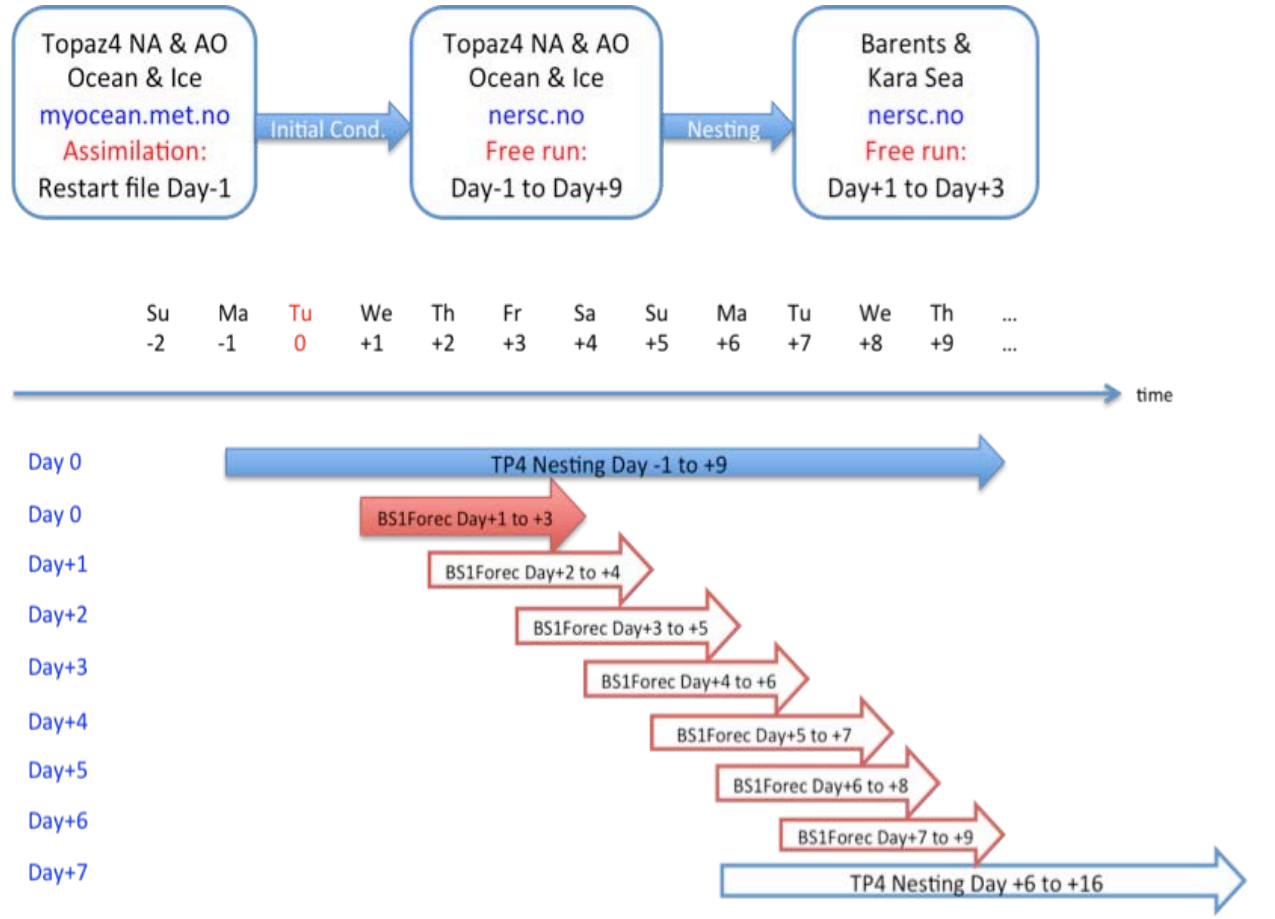

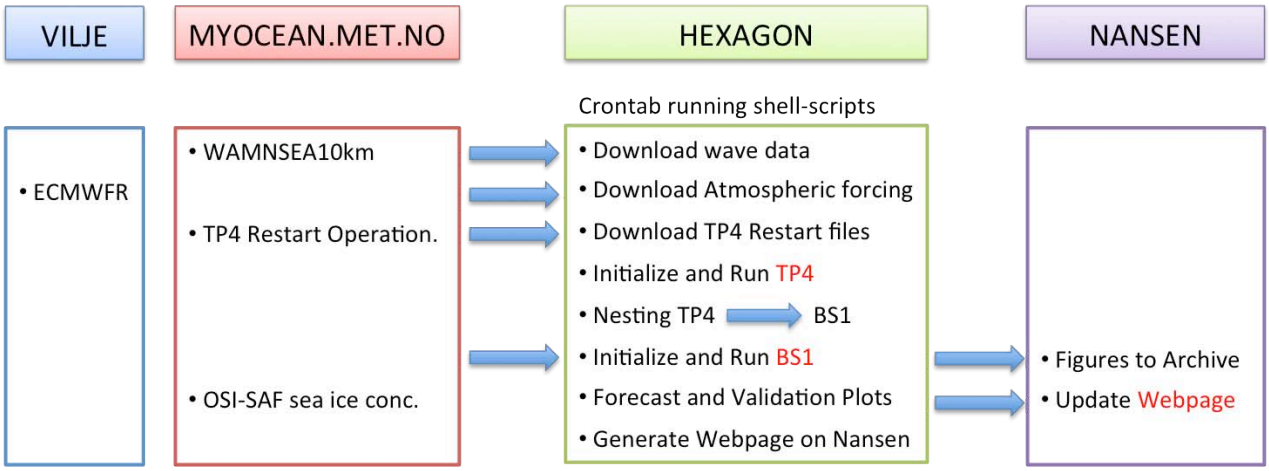

Figure 29. Upper graph: The cycle of the nested Barents and Kara Seas sea ice and ocean forecast system. Lower graph: . Schematics of computer resorces used for the forecast system

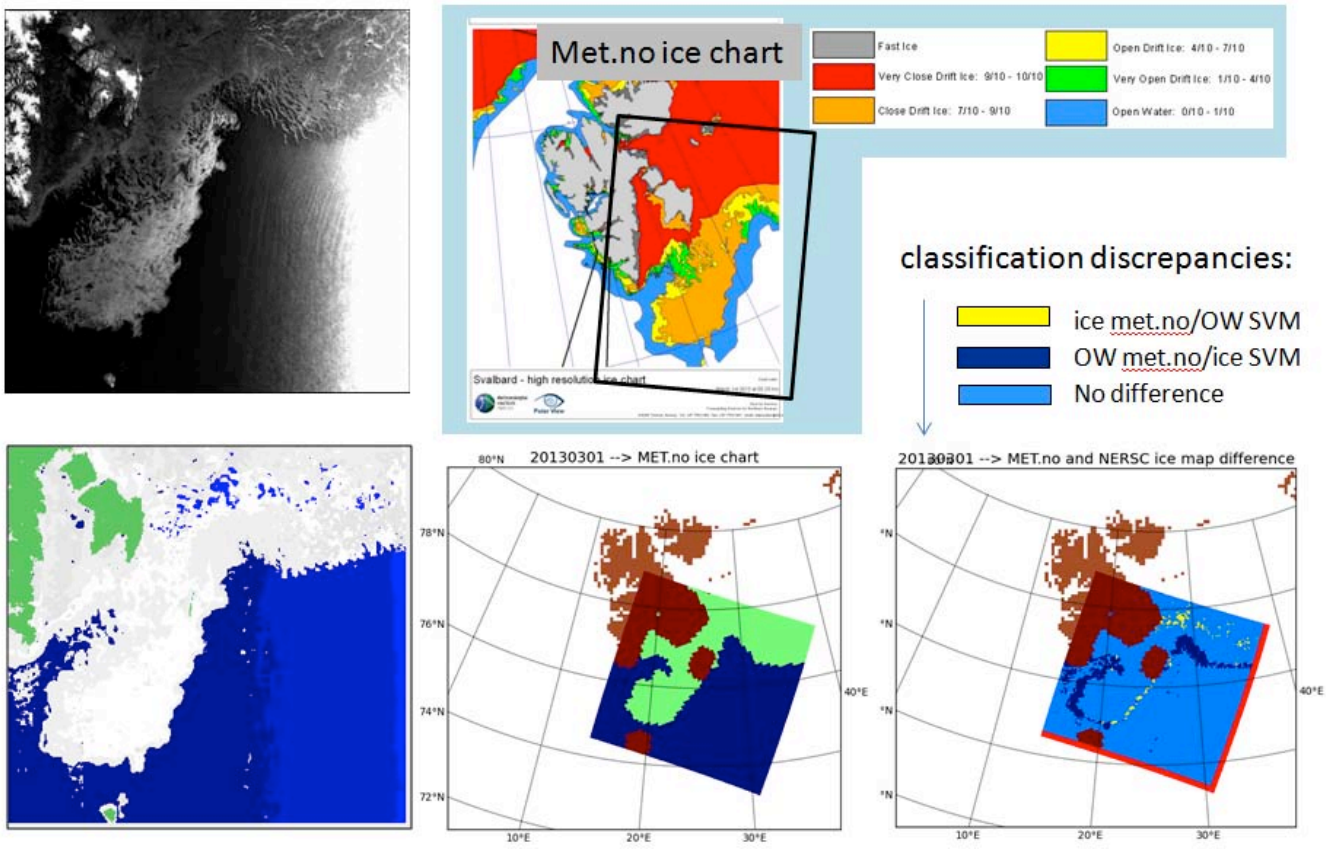

Fig. 30. Intercomparison of METNO and SVM ice charts for 01 March 2013.

month	Overall accuracy	OW_error	Ice_error
mar	0.92	0.06	0.02
apr	0.92	0.06	0.02
may	0.89	0.08	0.04
jun	0.87	0.11	0.02
jul	0.81	0.16	0.02
aug	0.86	0.12	0.01
sep	0.88	0.11	0.01
oct	0.94	0.05	0.01
nov	0.92	0.07	0.01

SVM ice classes / METNO ice classes	OW	Sea Ice	Unclassified
OW	OW accuracy	SVM sea ice class where there in OW in METNO	Unclassified pixels where there in OW in METNO
Sea Ice	SVM OW class where there is sea ice in METNO	Sea Ice accuracy	Unclassified pixels where there in sea ice in METNO

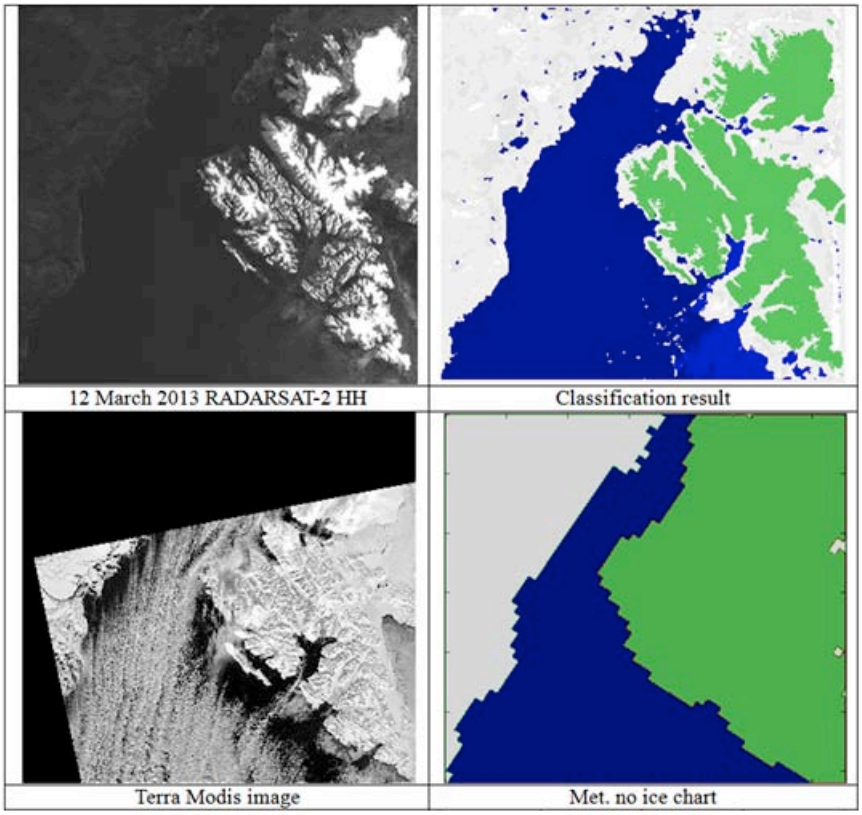

	OW	Sea ice	Un class
OW	96.07	1.67	2.26
Sea ice	6.20	92.83	0.97

Overall_accuracy = 94.24 %,

Figure 31. Upper left: SAR image from 12 March 2013 used in classification; upper right: classification results, lower left: Terra MODIS image, lower right: ice-water discrimination from Met.no's ice chart. The matrix shows the agreement between the two data sets in percent of the pixels in the image.

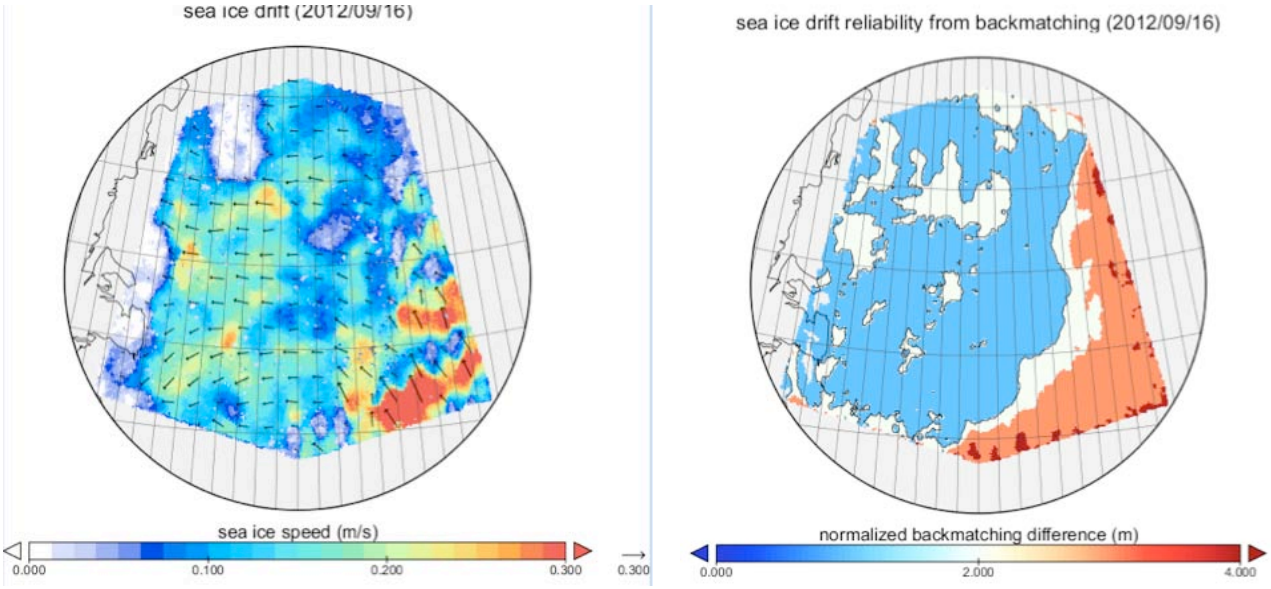

Figure 32. Left: Ice drift field form Radarsat-2 ScanSAR image in Fram Strait (16 Sept 2012); right: Reliability indicator from the ice drift vectors the left. Red and white areas are characterized by large back-matching differences, while blue regions are considered reliable.

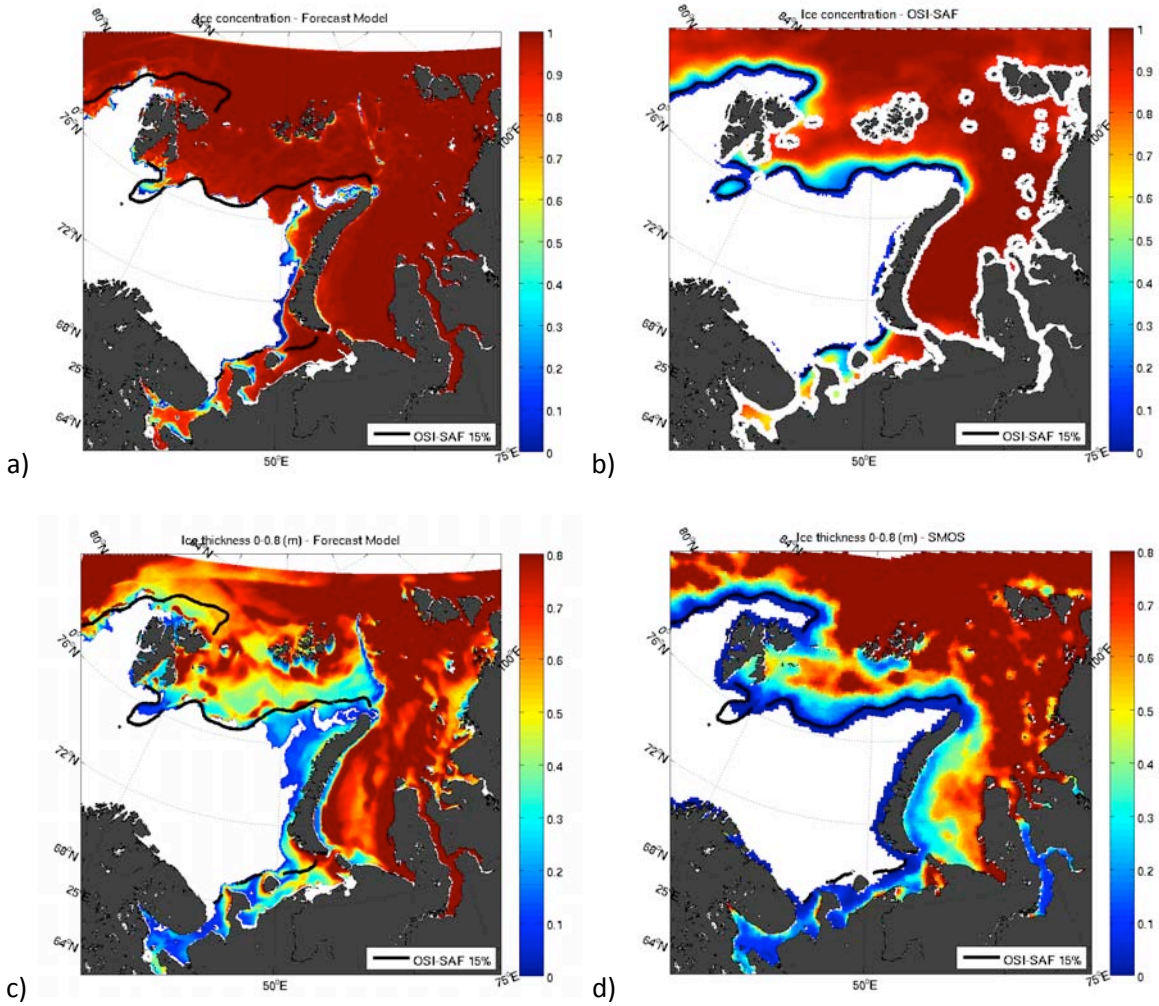

Figure 33. Comparing sea ice concentration from a) the model and b) OSI-SAF data and sea ice thickness from c) model and d) SMOSIce thin sea ice thickness.

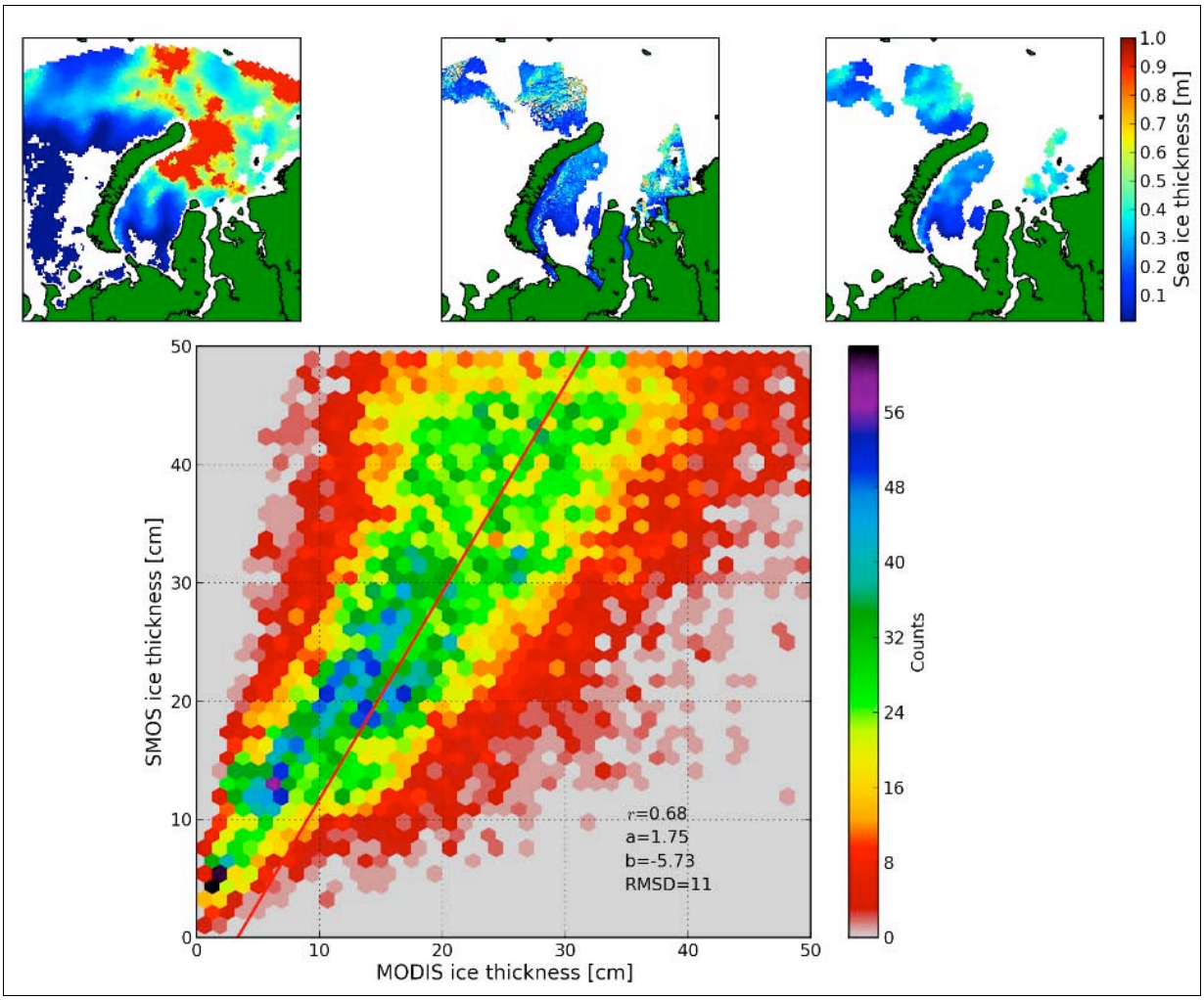

Figure 34. Comparison between SMOS (top left) and MODIS (top center) retrieved SIT for 4 Dec. 2010 in the Kara Sea. The valid MODIS data after averaging to the SMOS footprint size (top right). The scatter plot of MODIS and SMOS for all MODIS data from 24 Nov. 2010 to 14. Apr. 2011 (71 scenes) (bottom). Regression line (red): y = 1.75 x - 5.73, RMSD=11 cm, correlation of 0.68

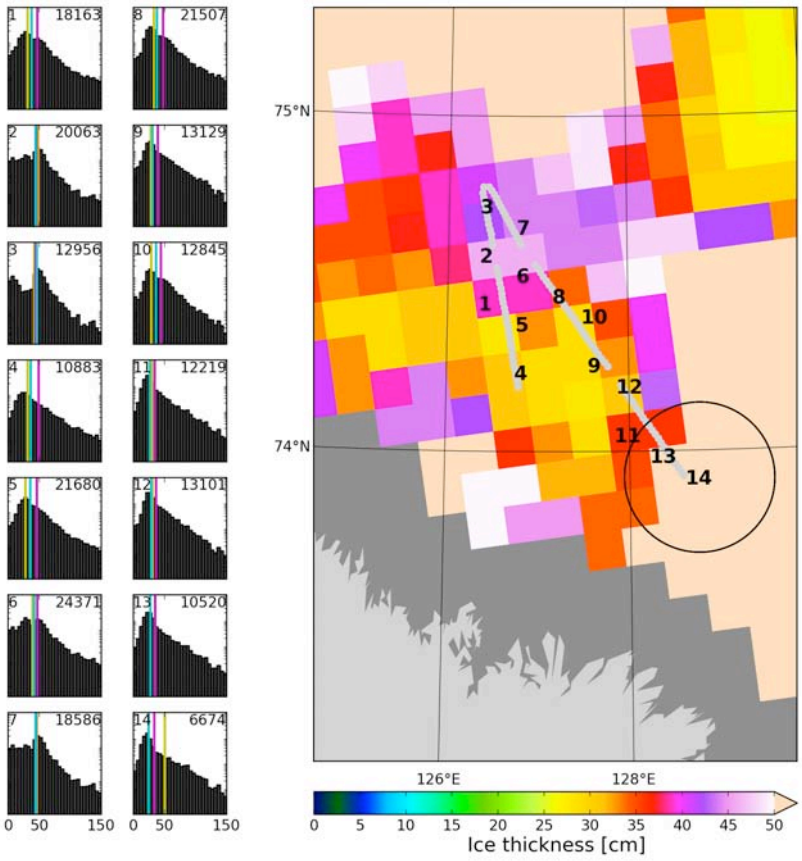

Figure 35. Comparison of EM Bird and SMOS sea ice thicknesses: (right panel) Location of EM bird flight of 20 April, 2012 (grey track) over SMOS retrieved ice thickness (colored background tiles). The large black circle illustrates the average size of a SMOS footprint; (left panel) Histograms of EM bird SIT retrievals within circular regions of SMOS footprint size centered around the same number (upper left of each histogram) on the right-hand image. The number of EM bird measurements for each histogram is shown on the upper right. The colored vertical lines correspond to the mean (purple) and median (cyan) of the EM bird measurements while yellow lines indicate the retrieved sea ice thickness by SMOS.

Table x: Datasets used for validation of the MPD algorithm (authors, location, year, method)

Polashenski, Barrow 2008	In situ field campaign, visual estimation
Polashenski, Barrow 2009	In situ field campaign, fractions along a 200m transect
Birnbaum, MELTEX 2008	Airborne measurements, supervised classification algorithm applied to geolocated quality assured aerial pictures
Birnbaum, NOGRAM 2011	Airborne measurements, supervised classification algorithm applied to geolocated quality assured aerial pictures
Scharien, Canadian Arctic 2002	In situ field campaign, visual estimation
Perovich, HOTRAX 2005	Ship cruise, hourly bridge observations, visual estimation

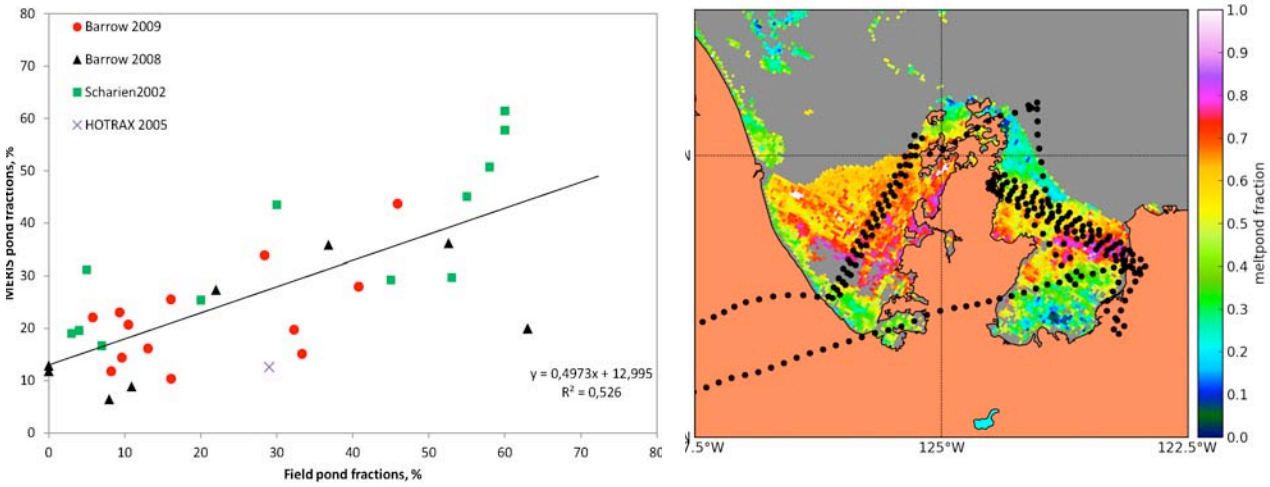

Figure 36: Validation of the MPD algorithm against (a) in situ pond fraction measurements, (b) airborne measurements (just one example from MELTEX 2008, 06.06.2008 is shown. Field value: on average 40% melt ponds).